



CHORUS

This is the accepted manuscript made available via CHORUS. The article has been published as:

Slip boundary conditions over curved surfaces

Lin Guo, Shiyi Chen, and Mark O. Robbins

Phys. Rev. E **93**, 013105 — Published 6 January 2016

DOI: [10.1103/PhysRevE.93.013105](https://doi.org/10.1103/PhysRevE.93.013105)

Slip Boundary Conditions over Curved Surfaces

Lin Guo¹, Shiyi Chen^{1,2}, and Mark O. Robbins^{1,3*}

¹*Department of Mechanical Engineering, Johns Hopkins University, Baltimore, MD 21218*

²*South University of Science and Technology, Shenzhen, China*

³*Department of Physics and Astronomy, Johns Hopkins University, Baltimore, MD 21218*

(Dated: December 9, 2015)

Molecular dynamics simulations are used to investigate the influence of surface curvature on the slip boundary condition for a simple fluid. The slip length is measured for flows in planar and cylindrical geometries with a range of wall-fluid interactions. As wall curvature increases, the slip length decreases dramatically for closely packed surfaces and increases for sparse ones. The magnitude of the changes depends on the crystallographic orientation and is different for flow along and perpendicular to the direction of curvature. These different patterns of behavior are related to the curvature-induced variation in the ratio of the spacing between fluid atoms to the spacing between minima in the potential from the solid surface. The results are consistent with a microscopic theory for the viscous friction between fluid and wall that expresses the slip length in terms of the lateral response of the fluid to the wall potential and the characteristic decay time of this response.

I. INTRODUCTION

Modern developments in micro- and nano-technologies have created great interest in studying and modeling fluid transport at these small scales. Solving continuum hydrodynamic equations requires boundary conditions at solid-fluid interfaces. As the system size shrinks to micro- or nano-scales, these boundary conditions play increasingly important roles because of the large surface-volume ratio. The traditional no-slip boundary condition for macroscopic flows may break down, and a slip boundary condition is then needed to describe the fluid velocity at the solid surface [1–5].

Navier proposed the first and the most widely used slip boundary condition [6], which states that the slip velocity is proportional to the shear rate of the fluid at the surface. The slip length is introduced as the proportionality coefficient, and is used to characterize the degree of fluid slip at the surface. In the simple case of flow past a flat surface, the slip length measures the distance from the actual surface to the virtual plane where the extrapolated fluid velocity would equal that of the solid surface.

Molecular dynamics (MD) studies for flat surfaces [7–12] have indicated that when the shear rate is small, the slip length is flow-independent and only depends on the properties of the fluid (e.g., viscosity, temperature, fluid structure) and the microscopic properties of the local interface (e.g., wall-fluid interaction strength, atomic structure of the surface). For surfaces with more complicated geometries, one can apply the Navier slip boundary condition locally with the same slip length but only if the surface normal changes on length scales that are much larger than the atomic scale and all the microscopic properties remain the same [13, 14]. This geometrical independence is of practical importance. For example, one can measure the local slip length from a surface with a simple

geometry (e.g., cylindrical for Surface Forces Apparatus experiments, spherical for atomic force microscopy experiments) [2, 3, 15, 16], and use it as the local intrinsic property for other surfaces as long as they are microscopically the same.

In the limit where the radius of curvature of the surface approaches the molecular-scale, the separation of the characteristic length scales fails and the small scale curvature becomes one of the microscopic properties of the surface. Some simulations suggest that curvature may affect the local slip length [17–20]. In particular, Falk et al. found very large changes with slip length in axial flow along nanotubes [19, 20]. A more recent study [21] argued that these nanotubes were so slippery that no velocity gradient occurred in the fluid and the effective slip length was infinite. The authors argued that slip was a material property and presented MD simulations that showed almost no change in slip length with curvature.

In this paper, we present MD simulations of slip over curved solids with a wide range of solid/fluid interactions and solid geometries. Curved walls are generated by smoothly rolling up planar walls into cylinders while preserving the local atomic structure of the surface. Studies of flow between cylinders give slip boundary conditions at walls with negative (outer) and positive (inner) curvature. Both axial flow along the cylinder and rotational Couette flow are studied.

We find very different changes in slip length with curvature for different surfaces and different flow directions. As curvature increases there can be little change in slip length, as found by Chen et al. [21], large decreases in slip length, as found by Falk et al., or increases in slip length. The key factor is the ratio of the lateral spacing between minima in the wall potential to the spacing between fluid atoms. Slip is suppressed when these spacings are comparable and fluid atoms can lock in registry with the substrate [7, 19, 20, 22, 23]. Curvature increases the spacing between minima, which may enhance or suppress locking. Since curvature does not affect the spacing along the cylinder axis, the change in slip length can be much

* mr@jhu.edu

greater for rotational flow around the cylinder than for axial flow.

All of the simulation results can be collapsed using a theory for friction between a solid and fluid layer [22, 23]. In this theory the key measure of the strength of viscous coupling between fluid and solid is the magnitude of lateral density modulations in the first fluid layer due to the periodic potential from the solid. Most of the variation in slip length with curvature is related to changes in this response. Slip also depends on the lifetime of these density modulations which is found to be a material property of the fluid, depending only on the ratio of the spacing between solid atoms to the mean spacing between fluid atoms. The relation between this theory and the later work of Falk et al. [19, 20] is discussed.

The paper is organized as follows. In Sec. II, the details of molecular dynamics simulations are described. In Sec. III, we describe how key quantities such as fluid layering, lateral structure factor and slip length are defined and measured from the simulations. In Sec. IV, results for slip length and fluid structure are presented and the behavior of the slip length is interpreted by a microscopic theory. The summary and conclusions are given in the last section.

II. DETAILS OF MOLECULAR SIMULATIONS

A. Interaction Potentials and Equations of Motion

We use standard molecular dynamics to simulate simple fluid flows over rigid solid walls. The simulations are performed using LAMMPS from Sandia National Laboratories ([24]). A truncated Lennard-Jones (LJ) potential is used to model the interactions between fluid atoms:

$$V_{LJ}(r) = 4\epsilon \left[\left(\frac{\sigma}{r}\right)^{12} - \left(\frac{\sigma}{r}\right)^6 \right] - V_c, \text{ for } r < r_c \quad (1)$$

where r is distance between the two atoms, and ϵ and σ define the characteristic energy and length scales of the fluid, respectively. V_{LJ} is truncated at a distance $r_c = 2.2\sigma$ to save computational cost, and V_c is chosen so that $V_{LJ}(r_c) = 0$. Wall (w) and fluid (f) atoms also interact through a truncated LJ potential with parameters ϵ_{wf} , σ_{wf} and $r_{c,wf}$. The four sets of wall-fluid interaction parameters studied are listed in Table I. If not stated otherwise, $\sigma_{wf} = 1\sigma$ and $r_{c,wf} = 2.2\sigma$.

The equations of motion are integrated using the velocity-Verlet algorithm with a time step $\Delta t = 0.005\tau$, where $\tau = \sigma\sqrt{m/\epsilon}$ is the characteristic time scale and m is the mass of a fluid atom. For most simulations, fluid temperature is maintained at $T = 1.1\epsilon/k_B$ by imposing a Langevin thermostat on all fluid atoms in the flow-irrelevant y -direction [7, 25]. The thermostatted equation of motion in the y -direction is given by

$$m\ddot{y} = f_{LJ} - m\Gamma\dot{y} + F(t) \quad (2)$$

Wall Type	ϵ_{wf}/ϵ	σ_{wf}/σ	$r_{c,wf}/\sigma$
A	0.1	1	2.2
B	0.4	1	2.2
C	0.4	1	1.12
D	0.057	1.27	2.2

TABLE I. The four sets of wall-fluid interaction parameters (subscript wf) studied in this paper. The energy ϵ_{wf} , interaction length σ_{wf} and cutoff distance $r_{c,wf}$ are normalized by the fluid interaction energy ϵ and length σ . The surface lattice spacing was $a/\sigma = 0.75, 0.86, 1.0, 1.09$ or 1.20 . For walls aligned with the (110) direction along the cylinder axis the inner and outer cylinder radii are 3.85σ and 23.0σ or 7.67σ and 26.83σ . For the (100) direction along the axis, the radii are 4.09σ and 21.69σ or 8.14σ and 25.75σ . The surface corrugation is decreased and slip length increased when ϵ_{wf} is decreased or σ_{wf} is increased.

where f_{LJ} is the total LJ force from all other particles. The damping rate Γ controls the heat flux between the system and the heat bath and $F(t)$ is a random force sampled from a Gaussian distribution with zero mean and variance $2m\Gamma k_B T/\Delta t$. We use a damping rate $\Gamma = 0.5\tau^{-1}$, which is small enough that the atomic motions are underdamped, but large enough to eliminate viscous heating. We checked that varying Γ by a factor of 2 does not change the results. Past studies of slip boundary conditions have shown there is little effect of thermostats on the low rate limit of interest here([7, 26, 27]). Effects are observed when rates are high enough that heating occurs([26, 27]).

For simulations of axial flow between cylinders, instead of the Langevin thermostat, an isotropic dissipative particle dynamics (DPD) thermostat with a damping rate $0.5\tau^{-1}$ is applied on the fluid [28-30]. Thus the angular invariance of the fluid flow is preserved. Changes in damping rate and comparison to the Langevin results for flat surfaces confirmed that this thermostat has negligible impact (<2%) on the presented results for flow, slip length and fluid structure.

The bulk density of fluid is fixed at $\rho = 0.81\sigma^{-3}$. The strain rates in our simulations are low enough ($\lesssim 0.07\tau^{-1}$) to ensure that the bulk fluid is Newtonian with shear viscosity $\mu \sim 2.13\epsilon\tau\sigma^{-3}$. In this low strain rate regime, linear response is also observed at the wall-fluid interface and the slip length is insensitive to shear rate [7, 8, 12, 21].

B. Planar Geometry

For the planar Couette geometry, fluid is confined in a channel between two solid walls parallel to the x - y plane (Figure 1(left)). Flow is generated by moving the top wall along x at a speed U_w . Periodic boundary conditions are imposed along x - and y -directions. Each pla-

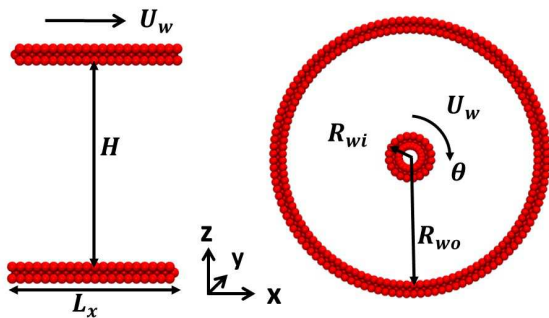


FIG. 1. (Color online) Geometry of planar (left) and cylindrical (right) geometries. In the planar case fluid is confined between rigid walls separated by height H and periodic boundary conditions are applied in the plane of the wall. Flow is generated by moving the top wall along x at a speed U_w . In the cylindrical case the walls are rigid coaxial cylinders with R_{wi} and R_{wo} the inner and outer radii of the solid surfaces, respectively. Angular and axial flow are generated by rotating the inner wall or translating it along the y -axis, respectively, so that surface atoms have speed U_w . Periodic boundary conditions are applied along the axial, y -direction.

nar wall consists of three (001) layers of a FCC crystal. Wall atoms are fixed rigidly to lattice sites. Past studies show thermal vibrations affect the value of slip length but do not change the trends with surface geometry and interactions [7, 11]. The x -axis is aligned with either the (110) or the (100) vector of the FCC lattice. We take the nominal height of the wall surfaces to coincide with the center of the wall atoms in the layer closest to the fluid. The separation distance between wall surfaces is $H = 30\sigma$. The spatial periods along x - and y - directions are $L_x = L_y = 24.08\sigma$ and $L_x = L_y = 25.54\sigma$ for cases of flow along (110) and (100) direction, respectively.

A key parameter of the wall is the lateral separation of the nearest neighbor atoms in the first layer, designated by the surface lattice spacing a . The surface lattice spacing determines the characteristic length of the atomic-scale corrugations in the wall potential felt by fluid atoms, and it has been disclosed to be an essential factor that regulates the degree of slip [7]. Here we investigate slip boundary conditions for four values of the surface lattice spacing on the bottom wall ($a = 1.20\sigma$, 1.09σ , 1.00σ , 0.86σ , and 0.75σ), and for various sets of the wall-fluid LJ parameters (Table I). The results serve as the reference cases for flat surfaces, i.e., curvature $\kappa = 0$. For top wall surfaces, no-slip boundary conditions are always enforced by using large values of ϵ_{wf} .

C. Cylindrical Geometry

As shown in Figure 1(right), fluid is confined in the region between two coaxial cylindrical walls, whose central axes lie along the y -axis. A periodic boundary condition

with a period of length $L_y = 24.08\sigma$ or 25.54σ is applied along the y - (axial) direction.

Each cylindrical wall is made by curving a planar wall along the x -direction, while the atomic arrangement remains unchanged along the y -direction. As depicted in Figure 2, the cylindrical wall is formed by three rolled-up layers of solid atoms, and the atoms of a given layer have the same radial distance from the central axis. Each layer consists of N_θ rows of atoms along the axial direction and the azimuth angle between neighboring rows is $2\pi/N_\theta$. The value of N_θ is chosen so that the surface layer adjacent to the fluid has a locally square structure with nearest-neighbor spacing a . Two orientations of the flat wall relative to the cylindrical axis are considered. In the first, the nearest-neighbor direction, (110), is aligned with the axis. In the second, the next-nearest neighbor direction (100) is aligned with the axis. Carbon nanotubes grow with a wide range of axis orientations and this is known to play an important role in determining their properties, such as conductivity [31–35].

The nominal position of the wall surface is defined by the first layer of wall atoms, such that the surface radius R_w equals the radial coordinate of surface atoms. The surface curvature κ is defined as $\kappa = 1/R_{wi}$ for the inner wall, and $\kappa = -1/R_{wo}$ for the outer one, where R_{wi} and R_{wo} denote the surface radii of the inner and the outer walls, respectively. In this study, for walls aligned with the (110) direction along the cylinder axis the inner and outer cylinder radii are 3.85σ and 23.0σ or 7.67σ and 26.83σ . For walls aligned with the (100) direction along the axis, the radii are 4.09σ and 21.69σ or 8.14σ and 25.75σ .

The procedure used to generate the curved walls may produce very small or large separations between atoms in the layers away from the fluid. These might lead to plastic rearrangements in experimental systems. However, the structure of these inner layers has very little effect on the flow boundary condition. Simulations without the third layer gave indistinguishable results for the slip length. The main effect of the second layer is to prevent fluid atoms from penetrating between atoms of the outer solid layer [7]. As shown in Sec. IV only the response to the periodic potential from the outer layer is needed to explain the detailed trends in slip length. This is why results for very short range interactions where fluid atoms only feel the outer layer ($r_c = 2^{1/6}\sigma$) show the same trends as simulations with larger r_c . It also explains why our results are very similar to those of Chen and Koplik [21] who used a very different crystalline structure under the outer solid layer.

D. Fluid Structure near Wall

Figure 3 shows the time-averaged fluid density profile as a function of distance from the wall for flat surfaces with $a = 1.2\sigma$ and 0.75σ . In the near wall region, the distribution of fluid atoms becomes non-isotropic and lay-

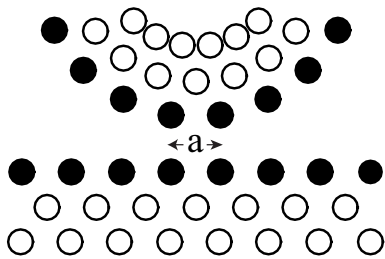


FIG. 2. Close up side views of the wall geometry for planar (bottom) and cylindrical (top) simulations with the nearest-neighbor direction aligned with flow. Circles show lattice sites and closed circles indicate atoms on the surface closest to the fluid. Surface atoms are separated by a and successive layers are separated by $a/\sqrt{2}$. The spacing between subsurface atoms changes with radius for curved surfaces.

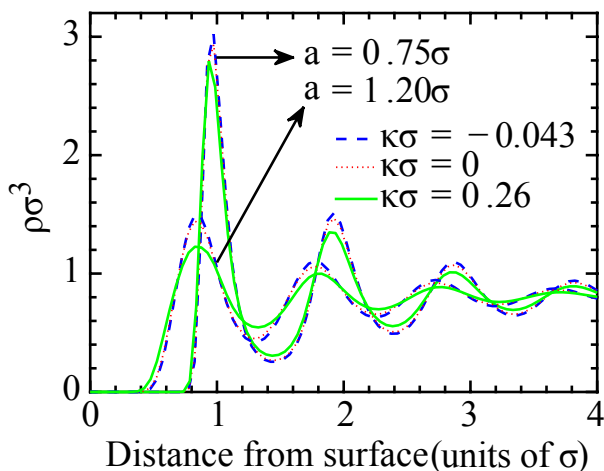


FIG. 3. (Color online) Fluid density as a function of distance from wall surface for lattice spacing $a = 1.20\sigma$ and 0.75σ at the indicated curvatures. Surfaces have wall-fluid interaction strength $\epsilon_{wf} = 0.4\epsilon$, $\sigma_{wf} = 1\sigma$, and the density is averaged over $10^4\tau$. The oscillations reflect layering and the layer boundaries are typically associated with the density minima. Here the (110) direction is along the cylinder axis but similar results are found for the (100) orientation.

ering emerges in the density profile [7, 10, 36–46]. The first peak corresponds to the preferred spacing between wall and fluid atoms. The density profile then oscillates with peaks separated by one fluid atom diameter, and gradually relaxes to a uniform bulk density after a few oscillations. Near a wall surface, layers can be associated with each density peak and the boundaries between layers with local density minima. Trends in layering with wall geometry and interactions are discussed in Sec. III B.

Layering is less related to the slip length than the degree of lateral structure within the first layer of fluid [7, 11, 12, 17, 19, 20, 43, 47–49]. To describe the in-layer structure, the 2D static structure factor, $S_1(\vec{q})$, is calculated as a function of wave vector \vec{q} for the first layer of fluid atoms.

For the flat surface, $S_1(\vec{q})$ is evaluated according to

$$S_1(\vec{q}) = S_1(q_x, q_y) = \left| \sum_j \exp[i(q_x x_j + q_y y_j)] \right|^2 / N_1, \quad (3)$$

where x_j and y_j are the 2D coordinates of atom j and N_1 is the number of fluid atoms in the first layer. The allowed wave vectors are determined by the periods of the system in the x - y plane, $\vec{q} = (2\pi h/L_x, 2\pi k/L_y)$ where h and k are integers. The periodic potential of the wall produces sharp peaks in $S_1(\vec{q})$ at the corresponding reciprocal lattice vectors $\vec{G}_{m,n}$ of the wall. For the fcc (100) surface with nearest-neighbors along x and y , $\vec{G}_{m,n} = (2\pi m/a, 2\pi n/a)$.

The squared relative amplitude of the areal density modulation $n_1(\vec{G})$ produced at each \vec{G} is

$$|n_1(\vec{G})/\bar{n}_1|^2 = \tilde{S}_1(\vec{G})/N_1 \quad (4)$$

where $\bar{n}_1 = N_1/A_1$ is the number of particles per area in the first layer. This response to the substrate potential is independent of system size while the intrinsic diffusive background $S_{1,eq}(\vec{G})/N_1$ decreases linearly with system size. We increase the system size until the diffusive background is small and then subtract it from the total signal. The induced peaks are confined to only one of the wave vectors allowed by periodic boundary conditions, and the background is obtained by averaging over the four closest allowed \vec{q} .

For the cylindrical surface, we approximate the first fluid layer by a 2D cylindrical sheet located at the radius corresponding to the first peak in the fluid density. As noted below this radius is associated with the flow boundary condition and is denoted R_{bc} . The polar coordinates of each atom in the first layer $(r\theta, y)$ are mapped to 2D coordinates on a sheet (x, y) with $x = R_{bc}\theta$ [19, 20]. Then the lateral structure factor is evaluated with respect to the 2D coordinates. The main difference from the planar case is that the period L_x is replaced by the circumference of the layer, $2\pi R_{bc}$, in determining the allowed wavevectors.

The structure factors shown below are obtained for equilibrium systems. They are nearly the same in sheared systems because the shear rates are kept in the limit of linear response. Structure factors are typically evaluated every 0.05τ and temporally averaged over up to 500τ .

E. Calculating the Slip Length

1. Planar Couette flow

For stationary Newtonian fluid flow past an impenetrable solid surface, Navier's slip model assumes that the friction force per unit area between the fluid and the solid surface is proportional to the slip velocity Δu_t , i.e., the relative velocity of fluid and solid. This force is balanced

by the viscous shear stress Π_{nt} of the fluid at the surface,

$$\beta \Delta u_t = \Pi_{nt}, \quad (5)$$

where β is the drag coefficient between the fluid and the solid surface, and n and t represent the normal and tangential directions to the surface, respectively. Newton's law for the bulk fluid relates the shear stress to the strain rate $\partial u_t / \partial n$:

$$\Pi_{nt} = \mu \frac{\partial u_t}{\partial n}. \quad (6)$$

where μ denotes the fluid viscosity. Combining these equations one arrives at Navier's slip boundary condition,

$$\Delta u_t = \frac{\mu}{\beta} \frac{\partial u_t}{\partial n} = L_s \frac{\partial u_t}{\partial n} \quad (7)$$

where the slip length $L_s \equiv \mu/\beta$ quantifies the degree of slip at the surface.

For planar Couette flow, the viscous stress Π_{xz} is constant throughout the channel, and the incompressible Navier-Stokes equations reduce to $\mu \partial^2 u_x / \partial z^2 = \partial \Pi_{xz} / \partial z = 0$. Solving this equation, one arrives at a linear velocity profile,

$$u_x = A_1 z + A_2. \quad (8)$$

The two constants, A_1 and A_2 , are determined by the boundary conditions at the wall-fluid interfaces.

Mean velocity profiles from two very different lattice constants are presented in Figure 4(a). Both profiles exhibit the expected linear velocity profile (Eq. (8)) in the central region of the fluid. Deviations begin to become apparent within one or two atomic diameters of the wall due to the layering and in-plane structure discussed above [7]. At the top wall there is a strong interaction that causes the fluid velocity to saturate to the wall velocity inside the fluid. This is called a stick boundary condition and is kept the same for all runs. The behavior near the stationary bottom wall is very sensitive to wall density. For the sparse surface case ($a = 1.2\sigma$) the velocity approaches zero, but for the closely packed surface there is a substantial velocity difference at the wall, i.e. slip.

The definition of the slip length in Eq. (7) requires both the strain rate and slip velocity. For Couette flow the strain rate is uniform in the central region and given by the coefficient A_1 in Eq. (8). The value of slip velocity is more ambiguous. Since the goal is to determine boundary conditions for the continuum equations, the slip velocity is evaluated from the extrapolation of the continuum solution rather than the actual velocity profile [5]. The answer still depends on the location of the wall which is uncertain up to lengths of order σ . We choose the height d_1 of the density peak associated with the first fluid layer (Fig. 3) as the hydrodynamic boundary. The slip velocity Δu_t then corresponds to the velocity difference between the first fluid layer and the solid wall. This

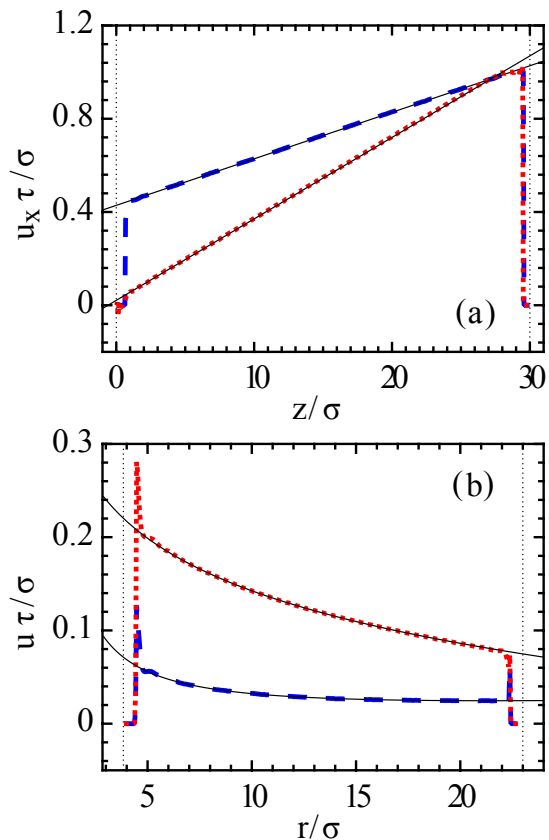


FIG. 4. (Color online) Velocity profiles for (a) planar Couette flow at $a = 0.75\sigma$ (dashed blue) and 1.2σ (dotted red), and (b) angular (dashed blue) and axial flow (dotted red) in cylindrical geometry at $a = 0.75\sigma$. Thin solid black lines show fits to continuum theory and dotted vertical lines show the positions of wall surface atoms. Flows are along the (110) orientation with $\epsilon_{wf} = 0.1\epsilon$.

is the natural quantity for Eq. (5) and the calculation of frictional drag discussed below. For the planar Couette case any other choice (e.g., in [7, 12, 50, 51]) gives a constant shift in the slip length and other common choices of the reference plane differ by less than the layer spacing.

For the planar flow simulations, the velocity profiles are averaged within horizontal bins of thickness $\Delta z = 0.05\sigma$ for a time period of $10^4\tau$ at steady state. The resulting flow profile is fit to Eq. (8) over the region more than 3σ from either surface. We verified that changing this condition by $\pm\sigma$ does not produce any noticeable changes. The slip length is then obtained from the fit coefficients as

$$L_s = d_1 + A_2/A_1 \quad (9)$$

The fit results are further averaged over 5 independent realizations of the system to quantify statistical errors and remove any long-time correlations.

2. Cylindrical Couette Flow

For the case of angular flow between rotating cylinders, the viscous shear stress at the curved cylindrical surface is given by

$$\Pi_{n\theta} = \mu \left(\frac{\partial u_\theta}{\partial n} - \kappa u_\theta \right) \quad (10)$$

where κ denotes the local curvature of the surface. For the convex inner surface in Figure 1, $\kappa > 0$, and for the concave outer surface, $\kappa < 0$. Plugging Eq. (10) into the force balance condition, Eq. (5), one arrives at the slip boundary condition for a curved surface [13, 14],

$$\Delta u_\theta = \frac{\mu}{\beta} \left(\frac{\partial u_\theta}{\partial n} - \kappa u_\theta \right) = L_s \left(\frac{\partial u_\theta}{\partial n} - \kappa u_\theta \right). \quad (11)$$

In terms of the local angular velocity, $\omega = u_\theta/r$, Eq. (11) can be rewritten into a form similar to Eq. (7) [21]:

$$\Delta \omega = L_s \frac{\partial \omega}{\partial n}. \quad (12)$$

Therefore the slip length along the direction of curvature can be interpreted as the distance inside the wall to which the fluid angular velocity is linearly extrapolated to reach the angular velocity of the wall surface.

For bulk flow between two rotating concentric cylinders, the incompressible Navier-Stokes equations reduce to

$$\frac{dp}{dr} = \rho \frac{u_\theta^2}{r}, \quad (13)$$

$$\frac{d}{dr} \left(\frac{1}{r} \frac{d}{dr} (r u_\theta) \right) = 0, \quad (14)$$

where the pressure p and the tangential velocity u_θ are functions only of the radial coordinate r and there is no flow along the cylinder axis. The general solution of the velocity profile is given by

$$u_\theta(r) = B_1 r + B_2/r, \quad (15)$$

where the constants B_1 and B_2 are determined by the boundary conditions.

In simulations, the angular flow is generated by rotating the inner wall at a rotation rate U_w/R_{wi} , where U_w is the speed of the surface atoms (closest to the fluid). For the cylindrical simulations, the velocity is averaged within cylindrical slabs of thickness $\Delta r = 0.05\sigma$ every $5 \times 10^3\tau$ over a simulation time of $10^5\tau$. The slip length is then calculated for each average velocity profile, and further averaged over 20 consecutive time intervals.

Figure 4(b) shows that the mean flow profiles from MD simulations are well fitted by the continuum solution except for regions within a few sigma of the walls (Eq. (15)). As found in past work, the viscosity of the fluid

may be modified in the layers closest to the walls ([7, 44, 52]). The sharp peak shown in Fig. 4 (b) near the inner wall comes from a very low density of atoms that are so close to the wall that their velocity is close to that of the wall. They make up a very small fraction of the first density peak. This effect is not visible near stationary walls because the density and wall velocity are both going to zero.

To measure the slip length from the MD velocity profiles, we rewrite Eq. (15) as

$$r u_\theta(r) = B_1 r^2 + B_2, \quad (16)$$

and fit the simulation data by this parabolic function. Combining Eq. (15) and Eq. (11), plugging in the fitted parameters B_1 and B_2 , and solving for L_s , the slip length of the inner wall is given by

$$L_s = - \left(B_1 R_{bc} + \frac{B_2}{R_{bc}} - U_{bc} \right) \frac{R_{bc}^2}{2B_2}, \quad (17)$$

where $R_{bc} = R_{wi} + d_1$ denotes the position of the hydrodynamic boundary, and $U_{bc} = U_w(1 + d_1/R_{wi})$ designates the fluid velocity at the effective hydrodynamic boundary R_{bc} . For the outer surface,

$$L_s = \left(B_1 R_{bc} + \frac{B_2}{R_{bc}} - U_{bc} \right) \frac{R_{bc}^2}{2B_2}, \quad (18)$$

where $R_{bc} = R_{wo} - d_1$, and $U_{bc} = 0$ since the outer wall is held at rest.

As for the planar case the wall position is defined at the center of the first density peak in the above analysis. For the cylindrical geometry, changing this definition does not produce a constant shift in the slip length because the flow is nonlinear. Shifting the reference plane to the midpoint between wall and first fluid layer ([19–21]) can reduce L_s by up to $\sim 4\sigma$ for the smallest radii and largest slip lengths but the trends with curvature remain the same. The definition used here is most natural for the theory described in Sec. IV which relates the friction between the first fluid layer and substrate to structure in the first layer.

3. Axial Flow in Cylindrical Geometry

For the axial flow case, the viscous shear stress at the cylindrical surface is $\Pi_{ny} = \mu \partial u_y / \partial n$ and thus the slip boundary condition has the same form as Eq. (7), $\Delta u_y = L_s (\partial u_y) / \partial n$. The Navier-Stokes equations for the bulk flow reduce to

$$\frac{\mu}{r} \frac{d}{dr} \left(r \frac{du_y}{dr} \right) = \frac{dp}{dy} = 0, \quad (19)$$

and the velocity profile is given by

$$u_y(r) = C_1 \ln(r) + C_2. \quad (20)$$

In simulations, the axial flow is produced by moving the inner cylinder along the y -direction at a speed U_w . To measure the slip length, Eq. (20) is fitted to the mean velocity profile (as illustrated in Figure 4(b)), and the slip length along the axial direction is calculated by

$$L_s = (C_1 \ln(R_{bc}) + C_2 - U_w) \frac{R_{bc}}{C_1}, \quad (21)$$

$$\text{and } L_s = -(C_1 \ln(R_{bc}) + C_2) \frac{R_{bc}}{C_1}, \quad (22)$$

for the inner and the outer wall, respectively.

III. RESULTS

A. Slip Length

Calculated slip lengths are tabulated in the supplementary material for all the flow geometries and surface properties included in this study [53]. For each case we verified that the results are in the low strain rate limit by varying the strain rate by at least a factor of two. The quoted values were evaluated for planar flows with top wall speed $U_w = 1.0\sigma/\tau$, for cylindrical angular flows with inner wall speed $U_w = 0.2\sigma/\tau$, and for cylindrical axial flows with inner wall speed $U_w = 0.6\sigma/\tau$. In all cases the maximum strain rate is less than $0.071/\tau$ which Chen et al. [21] also find is in the linear response limit.

In Figure 5(a), the value of the slip length is plotted against the surface curvature for cylindrical Couette flow with different surface lattice spacings. Here $\epsilon_{wf} = 0.1\epsilon$, $\sigma_{wf} = 1\sigma$ and flow is along the (110) direction between nearest neighbors of the fcc surface. For this rotational flow case, three typical patterns are clearly observed. For the highly packed surfaces, $a = 0.75\sigma$ or 0.86σ , the slip length L_s decreases by up to a factor of 5 as curvature increases. The opposite trend is observed for sparse surfaces, $a = 1.20\sigma$ or 1.09σ , where L_s increases slightly ($\sim 30\%$). Nonmonotonic behavior is found for $a = 1.00\sigma$: L_s drops as $\kappa\sigma$ increases from -0.043 to 0.13 and then rises as $\kappa\sigma$ further increases from 0.13 to 0.25 . These trends with curvature are determined by surface density and are not affected by changing the wall-fluid LJ interaction, although the absolute slip lengths are. Note that Chen et al. [21] considered $a = 1.09\sigma$ and positive curvatures. We also find little change in L_s for this special case.

The changes in slip length with curvature are very dependent on surface orientation as shown in Figure 5(b). For the nearest-neighbor (110) orientation, the slip length for rotational flow shows the large changes illustrated in Figure 5(a) while there is very little ($\sim 10\%$) change in the slip length for axial flow. In contrast, for the (100) orientation, curvature affects axial flow more strongly than rotational flow. Both follow the trend with curvature for rotational (110) flow but change more gradually. Note that for flat surfaces L_s is the same for flow

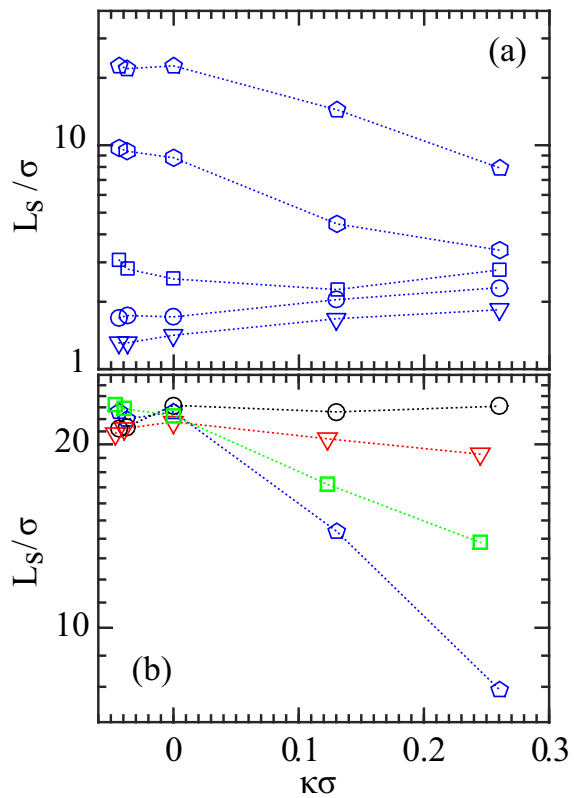


FIG. 5. (Color online) Slip length L_s as a function of surface curvature $\kappa\sigma$ for $\epsilon_{wf} = 0.1\epsilon$. (a) L_s for cylindrical Couette flows along (110) direction with different lattice spacing: $a = 1.2\sigma$ (triangles), 1.09σ (circles), 1.00σ (squares), 0.86σ (hexagons) and 0.75σ (pentagons). (b) L_s with $a = 0.75\sigma$ for cylindrical Couette flows along (110) (blue pentagons) and (100) direction (red triangles), and axial cylindrical flows along (110) (black circles) and (100) direction (green squares). Dotted lines are guides to the eye.

along (100) and (110) even though the directions are not crystallographically equivalent.

The different patterns of behavior of slip length for different flow directions, atomic spacings and lattice orientations can only be understood from the microscopic perspective. We first consider how curvature affects the structure of the fluid and then present a quantitative theory for the variations in slip length.

B. Fluid Structure

The correlation between the atomic spacing on flat surfaces and the degree of fluid layering has been discussed in Refs. [7, 10]. As illustrated in Figure 3, denser surfaces (smaller a) lead to sharper density peaks. One reason is that a higher density increases the number of wall atoms that interact with a given fluid atom and thus deepens the potential energy minimum at the first layer. Increasing the density also reduces the ability of fluid atoms to penetrate in between wall atoms. Figure 6(a,b) illustrate

the lateral variation of constant energy surfaces above flat walls. As wall atoms move closer, the depth of local minima decreases rapidly. The decrease in the corrugation of the equipotential surface reduces fluctuations in the preferred height of fluid atoms and thus sharpens the first density peak.

Figure 3 provides new information about how curvature affects layering. For all cases considered we found a monotonic increase in layering as the curvature went from positive to negative. The effect is particularly noticeable for large $\kappa\sigma$ where the radius of curvature approaches atomic scales. Figure 6(c) provides insight into the origin of this trend. While the spacing between wall atoms remains fixed, the first fluid layer forms at a different radius. Since the number of atoms is fixed, the spacing between potential minima scales as the radius of the fluid layer divided by that of the wall layer. This produces an effective decrease in the wall density with increasing $\kappa\sigma$. As for flat surfaces, the decrease in wall density leads to a broader and lower density peak.

Past work shows that the degree of slip correlates more strongly with lateral structure than fluid layering or wetting [7, 11, 12, 17, 19, 20, 43, 47–49, 54, 55]. Even featureless walls that are perfectly wetting produce strong layering peaks, but they provide a translationally invariant surface that cannot transmit friction. The drag coefficient β only depends on the variation in surface potential that is related to lateral corrugation (Figure 6). As noted in Sec. IID this lateral corrugation produces in-plane density modulations $n_1(\vec{G})$ (Eq. 4) at the reciprocal lattice vectors \vec{G} that characterize the periodicity of the substrate. The squared relative amplitude $|n_1(\vec{G})/\bar{n}_1|^2 = S_1(\vec{G})/N_1$.

Figure 7(a,b) show $S_1(\vec{q})/N_1$ for flat walls with high and low density. Only positive q_x and q_y are shown since the structure factor has the 4-fold symmetry of the wall. The weak circular ridges at a wave vector $|\vec{q}_f| \approx 2\pi/\sigma$ reflect the intrinsic short range order within a fluid. They are insensitive to wall density but decrease with system size as $1/N_1$ since $S_1(\vec{q}_f)$ is constant. There are also sharp peaks at the reciprocal lattice vectors characterizing the periodicity of the substrate. These Bragg peaks represent the response of the fluid to the surface corrugation and are independent of system size [7, 22, 23].

Previous studies of flat surfaces found that β increased with the in-layer response to the substrate potential at reciprocal lattice vectors Ref. [7, 22, 23, 54, 55]. For flat surfaces the largest response is at the shortest reciprocal lattice vectors, $\vec{G}_{\pm 1,0}$ and $\vec{G}_{0,\pm 1}$. As noted above, a denser surface tends to have a weaker corrugation and thus smaller values of $S_1(\vec{G})/N_1$. In Figure 7(a,b) the peaks for $a = 1.2\sigma$ are about 40 times larger than those for $a = 0.75\sigma$. Larger systems had to be used for $a = 0.75\sigma$ to reduce the circular ridge from the diffuse background below the Bragg peaks.

Figure 7(c,d) show $S_1(\vec{q})/N_1$ for the same atomic spacings but with curvature $\kappa\sigma = 0.26$. Here the cylinder axis is along the 110 direction and the curvature breaks the

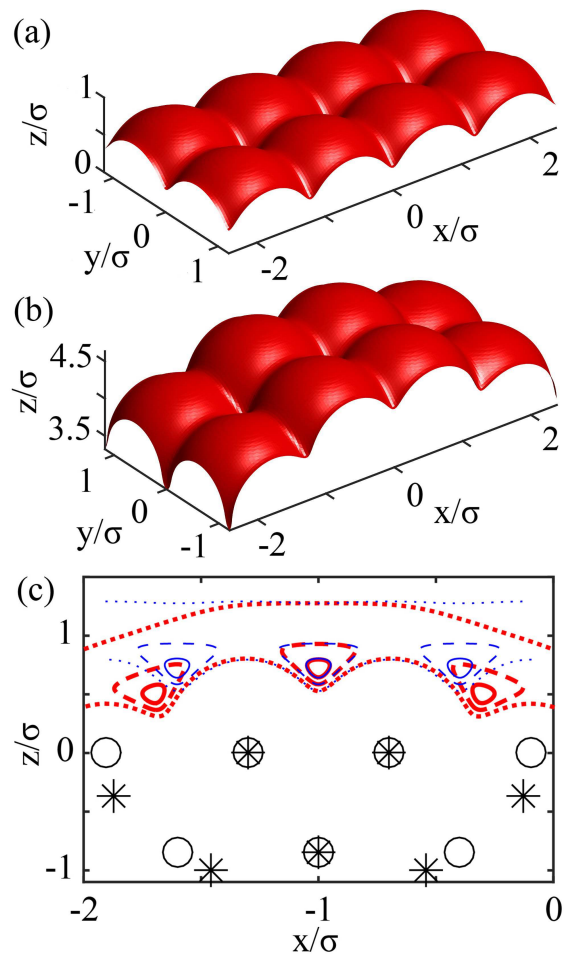


FIG. 6. (Color online) Equipotential surfaces at $V_{wall} = 1.1\epsilon$ for (a) planar wall and (b) cylindrical wall with positive curvature and radius $R_w = 3.84\sigma$. (c) Potential contours over the xz -plane at $y = 0$ for the same flat (thin blue) and cylindrical (thick red) surfaces presented in (a) and (b). Different line patterns correspond to different energy contours: $V_{wall} = -0.4\epsilon$ (solid), -0.3ϵ (dashed) and -0.1ϵ (dotted). The black circles and asterisks mark atomic positions of the flat and the cylindrical wall, respectively. The z coordinate is shifted so the topmost atoms of cylindrical and flat surfaces coincide. Here $\epsilon_{wf} = 0.1\epsilon$ and $a = 1.20\sigma$.

symmetry between x and y directions. The peaks along the axis of the cylinder change relatively little ($\sim 10\%$) from the values for flat surfaces, but the peaks along the direction of curvature change dramatically. From our previous arguments we expect the curvature to produce a larger effective spacing and thus a larger Bragg peak. This is consistent with the order of magnitude increase in the peak height for the dense surface, $a = 0.75\sigma$. However the Bragg peak for the sparse surface, $a = 1.2\sigma$, is smaller by about a factor of three. The reason is that the relative spacing of fluid and wall spacings is also important. The fluid can respond more to the potential when the Bragg peak is close to the circular ridge. Curvature moves the peak away from the ridge for $a = 1.2\sigma$ and

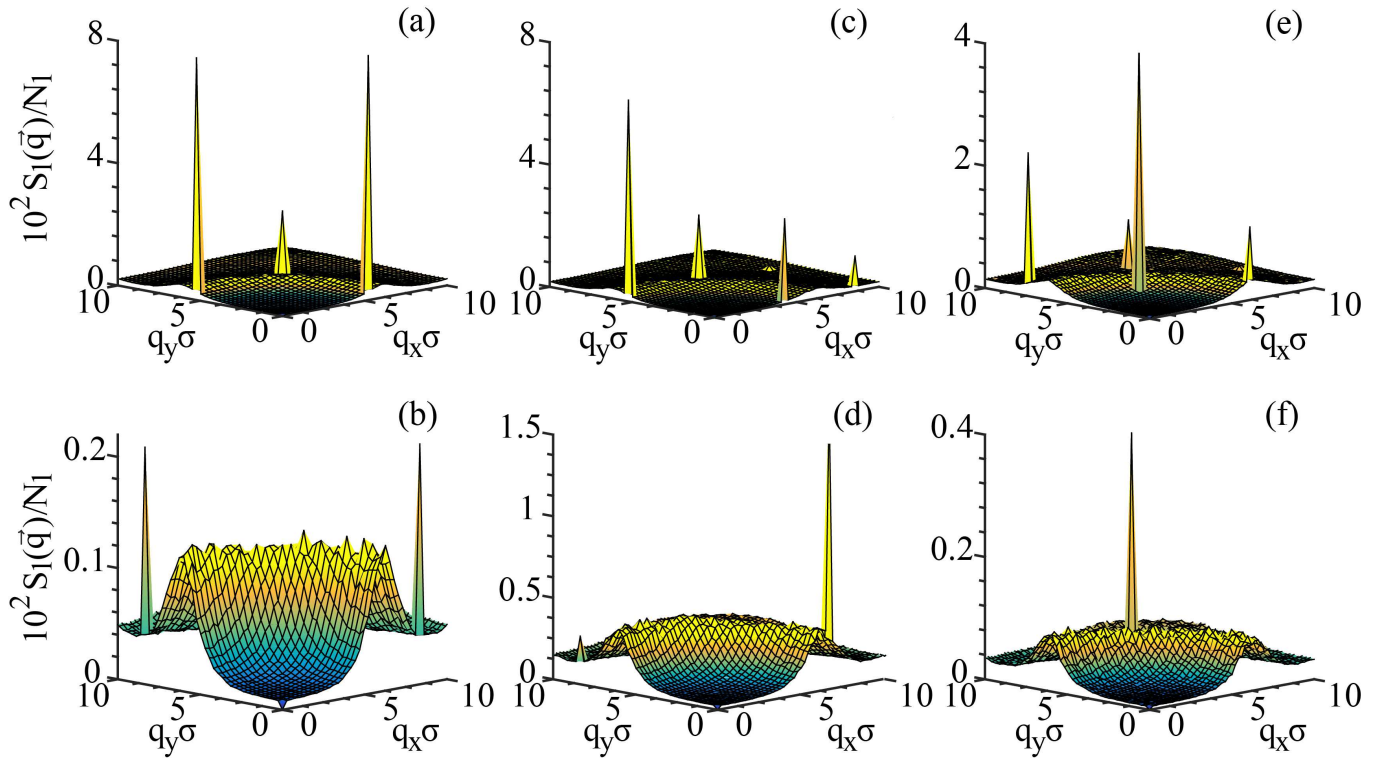


FIG. 7. (Color online) In-plane order as characterized by normalized structure factor $S_1(\vec{q})/N_1$ for two lattice spacings, $a = 1.20\sigma$ (a,c,e) and 0.75σ (b,f,d), with $\epsilon_{wf} = 0.1\epsilon$. (a) and (b) show results for flat walls with x-axes along (110). (c) and (d) show results for cylindrical walls with $\kappa\sigma = 0.26$ and axes along (110) direction. (e) and (f) show results for cylindrical walls with $\kappa\sigma = 0.24$ and axes along the (100) direction.

towards the ridge for $a = 0.75\sigma$.

In the following we focus on the wall induced portion of the Bragg peaks, $\tilde{S}_1(\vec{G})$. We verified that increasing the system size reduced the background from the circular ridge and did not affect the value of $\tilde{S}_1(\vec{G})$ obtained by subtracting this background. The calculated values of $\tilde{S}_1(\vec{G})/N_1$ at smallest reciprocal lattice vectors are also tabulated in the supplementary material for all the flow geometries and surface properties included in this study [53].

The variation of $\tilde{S}_1(\vec{G}_{1,0})/N_1$ with surface curvature κ is manifested in Figure 8 for (110) flow at different surface lattice spacings a . Note that the trends with curvature in $\tilde{S}_1(\vec{G}_{1,0})/N_1$ are exactly opposite to the trends in L_s shown in Figure 5(a). For dense surfaces the Bragg peak rises by an order of magnitude as curvature increases and the effective corrugation increases. For the sparse surfaces, the Bragg peak decreases monotonically because the associated wave vector is moving away from the circular ridge associated with the intrinsic spacing between fluid atoms. For the intermediate wall density the two effects compete and the peak height has a maximum at intermediate curvature.

The fundamental cause of these variations is the change in the effective spacing a_{eff} between potential energy minima divided by the intrinsic spacing between

fluid atoms. The spacing between fluid atoms scales as $\bar{n}_1^{-1/2}$ where \bar{n}_1 changes by of order 10% with interaction strength and other parameters. The effect of curvature on a_{eff} depends on orientation. For the (110) orientation the axial spacing is not affected while the spacing around the circumference scales as $a_{eff} = aR_{bc}/R_w = a(1 + \kappa d_1)$.

Figure 9(a) presents a clear picture of how the Bragg peak height varies against $a_{eff}\bar{n}_1^{1/2}$ for the full range of wall densities studied. Similar results are obtained for other wall/fluid interaction strengths. The largest response is obtained for $a_{eff}\bar{n}_1^{1/2}$ around 0.8 to 0.9, where the Bragg peak is near the center of the circular ridge. The peak height falls off as a_{eff} increases or decreases because the peak position moves away from the intrinsic fluid spacing. The decrease in corrugation with decreasing a_{eff} produces a very asymmetric curve that drops much more rapidly as a_{eff} decreases. Note that curvature does not change a_{eff} along the cylindrical axis for the 110 orientation and we observe little ($< 10\%$) change in $\tilde{S}_1(\vec{G}_{0,1})/N_1$ with κ . Figure 9(b) replots the data from Figure 5(a) as a function of a_{eff} . Note that the trends in L_s are exactly opposite to those in $\tilde{S}_1(\vec{G})/N_1$. Stronger order induced by the solid leads to less slip.

The effect of curvature on $\tilde{S}_1(\vec{G})/N_1$ is quite different for the (100) orientation where flow is along the next-

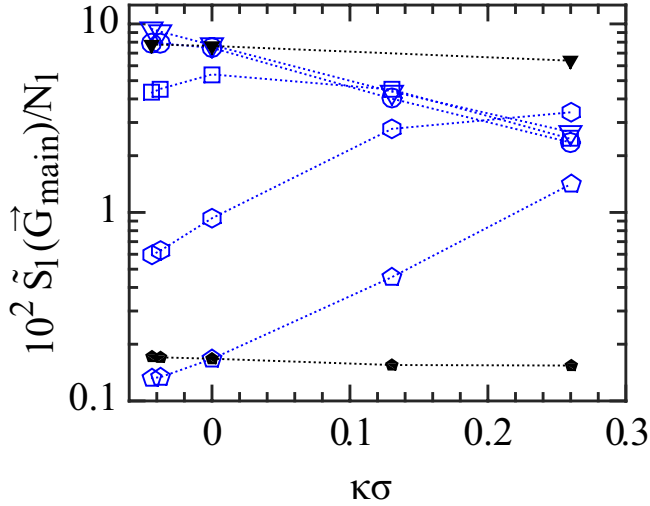


FIG. 8. (Color online) Variation of $\tilde{S}_1(\vec{G}_{1,0})/N_1$ (open blue) and $\tilde{S}_1(\vec{G}_{0,1})/N_1$ (closed black) with surface curvature for the same surfaces shown in Fig. 5(a), i.e., $\epsilon_{wf} = 0.1\epsilon$ and lattice spacing $a = 1.2\sigma$ (triangles), 1.09σ (circles), 1.00σ (squares), 0.86σ (hexagons) and 0.75σ (pentagons). Dotted lines are guides to the eye.

nearest neighbor direction. Curvature now rotates the direction θ between the cylinder axis and the nearest potential energy minima as well as changing the distance. Accounting for the change in spacing around the circumference we find:

$$a_{eff} = a(1 + \kappa d_1 + \kappa^2 d_1^2)^{1/2} \sim a(1 + \kappa d_1/2) \quad (23)$$

$$\tan(\theta) = 1/(1 + \kappa d_1) \sim 1 - \kappa d_1 \quad (24)$$

Figure 7(e,f) show $S_1(\vec{q})/N_1$ for the same curvature as Figure 7(c,d) but with this new orientation. As expected, the smaller change in a_{eff} leads to smaller changes in the Bragg peak heights. This is also consistent with the smaller change in L_s with curvature for this wall orientation. Note that the reciprocal lattice vectors rotate in the opposite direction from the vector to adjacent potential energy minima and thus towards the cylinder axis. As we now discuss, this change in direction explains why curvature affects axial flow more strongly than rotational flow for the (100) direction.

C. Relating Slip Length to Structure

In this section, we describe a microscopic theory that provides a quantitative relationship between the slip length, curvature and fluid structure, and thus gives a deeper insight into the mechanism of the wall-fluid coupling. By definition, the slip length L_s is the fluid viscosity divided by the interfacial drag coefficient. We have verified that for our simulations the viscosity can be treated as a constant parameter. Thus, the slip length is only a function of the strength of the viscous friction at

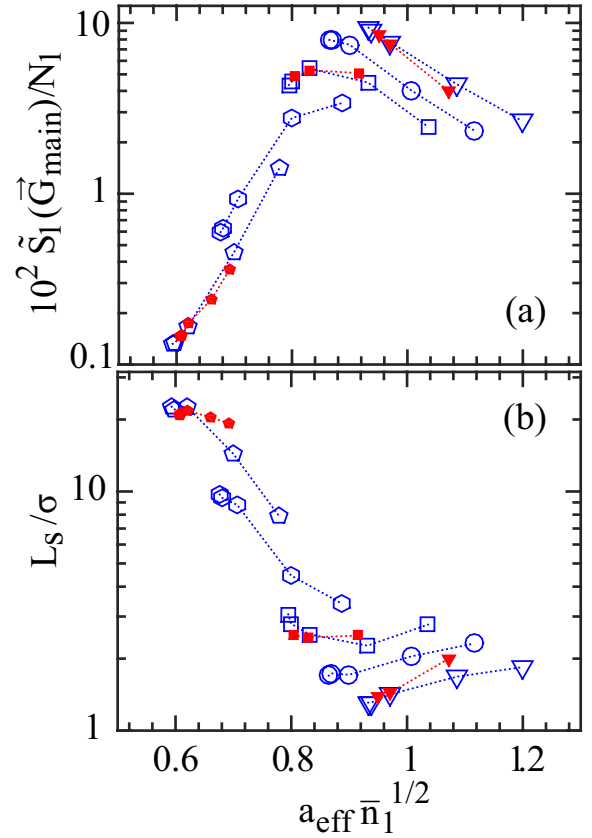


FIG. 9. (Color online) (a) Variation of $\tilde{S}_1(\vec{G})/N_1$ at $\vec{G}_{1,0}$ for y-axis (110) orientation (open blue) and at the smallest \vec{G} for y-axis along (100) orientation (closed red) as a function of the relative effective spacing $a_{eff}\bar{n}_1^{-1/2}$, i.e., the effective spacing of minima in the wall potential energy a_{eff} normalized by the mean spacing of the first layer $\bar{n}_1^{-1/2}$. The symbols indicate lattice spacing $a = 1.2\sigma$ (triangles), 1.09σ (circles), 1.00σ (squares), 0.86σ (hexagons) and 0.75σ (pentagons). (b). Variation of L_s as a function of effective spacing for cylindrical Couette flow and for the same surfaces in (a). Dotted lines are guides to the eye and $\epsilon_{wf} = 0.1\epsilon$.

the wall-fluid interface, i.e., L_s varies inversely proportional to the drag coefficient β .

The force between the wall and the first fluid layer dominates the drag force. It can be calculated using a model for the closely related problem of friction between an adsorbed monolayer and a solid substrate [22, 23, 54, 55]. While the fluid layer slides over the substrate, the density modulation produced by the periodic substrate potential remains locked in phase with the substrate. The relative motion of the wall-induced modulation and the center of mass of the layer leads to dissipation and thus a viscous drag. The rate of energy dissipation is proportional to the energy stored in the modulation and to the decay rate of energy into other modes. Equating this dissipation to the power per unit area dissipated by drag, $\beta\Delta u^2$, gives an expression for β and an associated time $\tau_{slip} = m\bar{n}_1/\beta$.

Smith et al [23] present expressions for β in the limit of linear response where the modulation in areal number density at wave vector \vec{q} and frequency ω , $n(\vec{q}, \omega)$, is proportional to the substrate potential $U(\vec{q}, \omega)$:

$$n_1(\vec{q}, \omega) = -\alpha(\vec{q}, \omega)U(\vec{q}, \omega) \quad (25)$$

where $\alpha(\vec{q}, \omega)$ represents a linear susceptibility to the substrate potential. Their Eq. (10) gives

$$\beta = \sum_{\vec{G}} |U(\vec{G})|^2 |\hat{G} \cdot \Delta \hat{u}|^2 |\vec{G}|^2 \frac{\text{Im}[\alpha(\vec{G}, \vec{G} \cdot \Delta \vec{u})]}{\vec{G} \cdot \Delta \vec{u}}, \quad (26)$$

where $\vec{G} \cdot \Delta \vec{u}$ represents the oscillation frequency produced by relative motion at slip velocity $\Delta \vec{u}$ and the last term on the right side becomes independent of $\Delta \vec{u}$ as $\Delta \vec{u}$ goes to zero. \hat{G} and $\Delta \hat{u}$ are unit vectors along \vec{G} and $\Delta \vec{u}$, respectively. Note that β scales as the square of the Fourier components of the substrate potential. Refs. [22, 23] tested this scaling over 3 orders of magnitude in β . One of the complexities associated with using Eq. (26) is that the substrate potential depends upon height. One can calculate the Fourier transform averaged over the density profile in the first layer or one can use the Bragg peaks in the structure factor to measure the effective potential. Using the general relation

$$\frac{\tilde{S}_1(\vec{G})}{N_1} = \left| \frac{n_1(\vec{G}, 0)}{\bar{n}_1} \right|^2 = \left| \frac{\alpha(\vec{G}, 0)}{\bar{n}_1} \right|^2 |U(\vec{G})|^2, \quad (27)$$

one can rewrite the drag coefficient as

$$\beta = \bar{n}_1 \sum_{\vec{G}} |\hat{G} \cdot \Delta \hat{u}|^2 \frac{\tilde{S}_1(\vec{G})}{N_1} \frac{1}{t_{ph}(\vec{G})}, \quad (28)$$

where

$$t_{ph}(\vec{G}) \equiv \lim_{\omega \rightarrow 0} \frac{m}{\bar{n}_1 |\vec{G}|^2} \frac{\omega |\alpha(\vec{G}, 0)|^2}{\text{Im}[\alpha(\vec{G}, \omega)]}, \quad (29)$$

can be interpreted as the lifetime of acoustic phonons in the fluid layer [23], and is inversely proportional to the rate at which the energy stored in this induced modulation is dissipated into other density waves. The first factor in the sum of Eq. 28 reflects the fact that only modulations with a component along the direction of flow $\Delta \hat{u}$ are affected by the motion and contribute to dissipation.

Eq. (28) explains many of the trends found above, including the inverse correlation between $S_1(\vec{G})$ and L_s seen in Figure 8 and in previous studies of flat surfaces [7, 11, 12, 43, 47–49, 56]. In the case of flat surfaces the predicted slip length is independent of direction by symmetry (Table S3). For example for flow along the (110) orientation two of the four reciprocal lattice vectors are along the flow and contribute to β while the others are perpendicular. For the (100) orientation, all four contribute to β but only half as much, since they are at 45

degrees to the flow. Curvature breaks this symmetry. For the (110) orientation, curvature only affects the magnitude of \vec{G} and $\tilde{S}_1(\vec{G})$ along the rotation direction. This explains why rotational slip lengths change but axial do not. For the (100) orientation all four \vec{G} change in magnitude and all have the same $\tilde{S}_1(\vec{G})$. Thus the axial and rotational slip lengths change in the same direction. The axial slip length is smaller because \vec{G} rotates to be more along the axial direction (Eq. 24).

In the cases considered in Refs. [22, 23], the phonon lifetime was nearly constant and the slip length scaled inversely with the sum over the smallest wave vectors of $\tilde{S}_1(\vec{G}_{main})/N_1$. Figure 10(a) shows there is a strong inverse correlation between slip length and $\tilde{S}_1(\vec{G})/N_1$ for all curvatures and orientations considered. However there is a significant spread that must reflect a variation in t_{ph} .

Figure 10(b) shows the value of the phonon lifetime calculated from Eq. (28) as a function of the ratio between minima spacing and fluid atom spacing, $a_{eff}\bar{n}_1^{1/2}$. All the data collapse onto a universal curve that represents the intrinsic response of the fluid layer. This represents a very compelling confirmation of Eq. (28).

We have attempted to calculate t_{ph} independently by measuring the susceptibility to a sinusoidal potential. As discussed in the Appendix, the potential oscillated with time but was constant for heights below the first minimum in the density shown in Fig. 3. For $a = 1.0$ ($a_{eff}\bar{n}_1^{1/2} = 0.82$) we find $t_{ph}/\tau = 0.92$, which is in excellent agreement with the numerical results in Fig. 10(b). However, for $a_{eff}\bar{n}_1^{1/2} = 0.6$ and 1.0 the calculated values of t_{ph} are much larger than the numerical results, $t_{ph}/\tau = 0.62$ and 0.61, respectively. This deviation reflects the fact that Equations 25 to 28 assume that the density modulations in the first layer are independent of height. This assumption is reasonably accurate for $a_{eff} = 1.0$ but there are strong variations with height for larger and smaller a_{eff} .

Figure 11 shows the cosine Fourier transform $n(\vec{G})$ of the local area density as a function of height for flat surfaces of different a . A negative value corresponds to density peaks out of phase with the solid substrate so that fluid atoms lie in gaps between solid atoms. Positive values correspond to fluid atoms lying above solid atoms.

For $a = 1.00\sigma$ the order is similar to that in an fcc crystal with all atoms in the first fluid layer above gaps in the solid. Atoms in the second layer lie above gaps in the first layer and thus above solid atoms. For smaller and larger a the oscillations in in-plane order do not correspond with the peaks and troughs in the density vs. height. The sign of $n(\vec{G})$ changes within the first layering peak in both cases. Indeed for $a = 0.75\sigma$ the sign change occurs near the density peak of the first layer. The transition to $n(\vec{G}) > 0$ indicates that the atoms are not responding to the direct interaction with the wall, but instead to the density modulation in fluid atoms that lie closer to the wall where $n(\vec{G}) < 0$. The lack of coher-

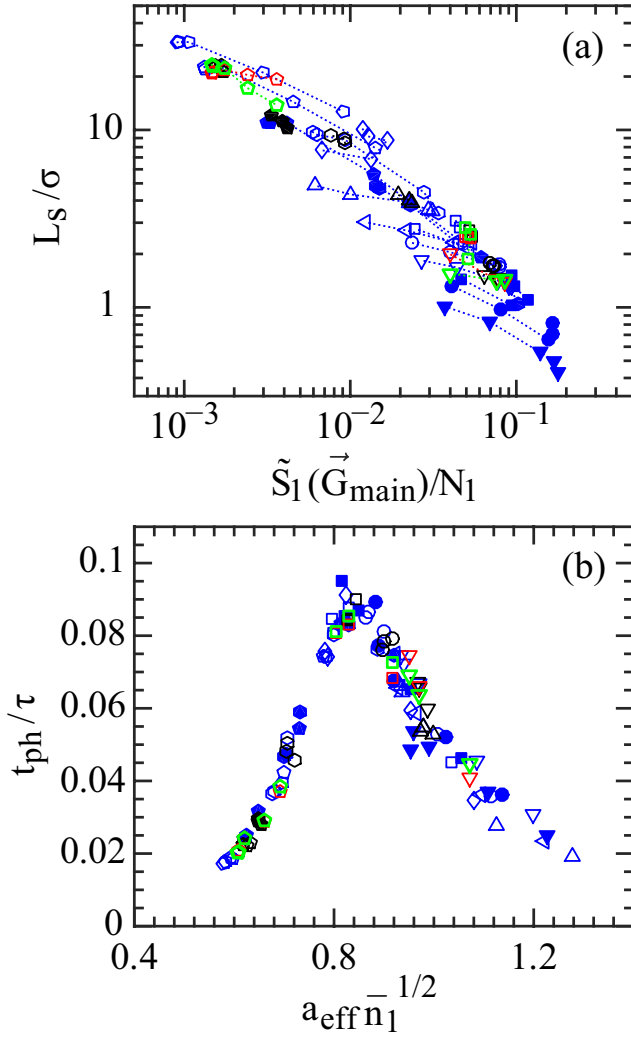


FIG. 10. (a) Variation of slip length L_s as a function of the first peak in the structure factor $\tilde{S}_1(\vec{G}_{main})/N_1$ for cylindrical Couette flows along (110) (blue) and (100) (red) directions, and axial cylindrical flows along (110) (black) and (100) (green) directions. Results are shown for lattice spacing $a = 1.2\sigma$ (triangles), 1.09σ (circles), 1.00σ (squares), 0.86σ (hexagons) and 0.75σ (pentagons) and different wall-fluid interactions from Table I: A (open), B (closed), C (right-side left triangle and pentagon) and D (diamond and right-side up triangle). Dotted lines are guides to the eye. (b) Variation of phonon lifetime t_{ph} from Eq. 28 with $\tilde{S}_1(\vec{G})$ integrated over the entire first layer as a function of the relative effective spacing $a_{eff} n_1^{1/2}$.

ence in the first density peak reduces the lifetime of the associated mode and thus t_{ph} is smaller than in the two dimensional approximation of Eq. 29.

It is possible to choose different definitions of the layer width that improve the quantitative agreement with Eq. (28). For example, choosing the top of the first layer to coincide with the height where $n(\vec{G})$ first becomes positive, improves quantitative agreement in all cases. How-

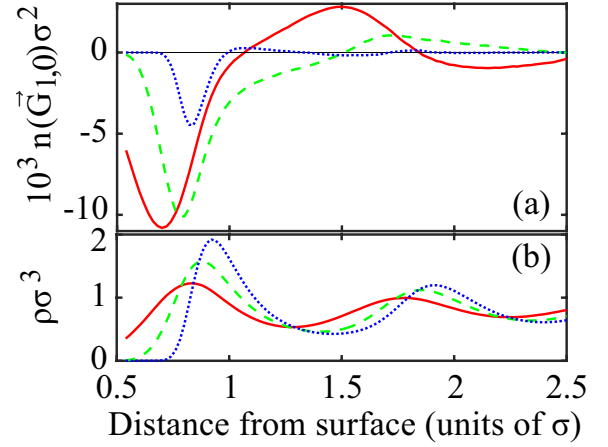


FIG. 11. (Color online) (a) Variation of cosine Fourier transform $n(\vec{G})$ of the local area density (averaged over a thin slice) as a function of height for flat surfaces where $\epsilon_{wf} = 0.1\epsilon$ and $a = 1.2\sigma$ (red), 1.00σ (green), and 0.75σ (blue). The dotted line designates $n(\vec{G}) = 0$. (b) Fluid density profiles for the same surfaces.

ever, deviations for large a_{eff} remain larger than the statistical uncertainties.

In Refs. [19, 20], the drag coefficient β along the axial direction was explored for carbon nanotubes. They used a fluctuation dissipation argument that is closely related to the above discussion in the linear response limit. They find

$$\beta = \frac{t_F \bar{n}_1}{k_B T} \sum_{\vec{G}} S_{1,eq}(\vec{G}) f_1^2(\vec{G}), \quad (30)$$

where t_F is the force decorrelation time at equilibrium and $f_1(\vec{G})$ is the Fourier component of the force field along the flow direction. They did not specifically state that the equilibrium structure factor rather than the induced peak should be used in Eq. (30) but the density modulations were too small to influence $S_1(\vec{G})$ in their system and this identification is consistent with their discussion.

Note that Eq. (30) has many similarities to Eq. (26). Since $f_1(\vec{G}) = U(\vec{G})(\vec{G} \cdot \Delta \hat{u})$, both expressions predict quadratic scaling of beta with substrate potential. This is the lowest order scaling allowed by symmetry and the quadratic scaling was confirmed in Refs. [22, 23] over 3 orders of magnitude in β . As discussed above, $S_{1,eq}(\vec{G})$ is related to the response to the substrate potential.

In the Appendix we show that Eq. (30) is quantitatively consistent with both L_s and the theory of Smith et al. (Eq. (28)) for a model potential that is uniform throughout the first layer. However for the actual atomistic potential, Eq. (30) is less accurate because of the variations in order shown in Fig. 11. Falk et al. [20] note that the rapid decay of the potential corrugation with height lead to a quantitative discrepancy from their theory by a "constant prefactor of 10 or less, depending

on the liquid". The Appendix shows that the prefactor may depend on the solid as well as the liquid. We also show that the initial fluctuation-dissipation argument that leads to Eq. (30) breaks down for atomistic interactions.

IV. SUMMARY AND CONCLUSIONS

We have used molecular dynamics simulations of flows in planar and cylindrical geometries to study the variation of the slip length with surface curvature for a range of geometries and surface interactions. Curvature at nanometer scales can increase or decrease L_s by an order of magnitude, depending on the direction of flow and surface geometry. The results explain why little change in L_s was seen in one previous study [21] while another found large changes [19, 20].

The slip length scales inversely with the viscous drag β between the first fluid layer and the solid wall, $L_s = \mu/\beta$. As in previous studies of flat surfaces [7, 11, 12, 17, 19, 20, 43, 47–49], the drag is directly related to lateral density modulations induced in the fluid by the wall potential. The magnitude of this epitaxial order increases with the strength of the corrugations in the wall potential and also with the susceptibility of the fluid to respond to the potential. This susceptibility is greatest when the separation between minima in the potential is comparable to the spacing between fluid atoms in the first layer.

Curvature changes the effective separation a_{eff} between minima because the fluid atoms lie at a different radius than the solid substrate. As shown in Fig. 6, positive curvature increases the spacing because fluid atoms are at a larger radius, while negative curvature decreases the spacing. The fractional change in the spacing between potential minima is $\sim \kappa d_1$ where d_1 is the height of the first fluid layer above the solid.

A natural measure of the ratio between the spacing of minima and the spacing between fluid atoms is $a_{eff}n_1^{1/2}$ where n_1 is the areal density of fluid atoms in the first layer. Independent measures of the susceptibility (see Appendix) show that the fluid is most able to lock into the potential corrugation when $a_{eff}n_1^{1/2} \approx 0.8$ and drops as a_{eff} increases or decreases. Fig. 12 shows that the slip length is smallest (β is largest) at slightly larger a_{eff} and changes much more rapidly with decreases in a_{eff} than increases in a_{eff} . This asymmetry reflects changes in the strength of the periodic corrugation from the substrate. Increasing the spacing between solid atoms allows fluid atoms to penetrate more deeply into the spaces between them and greatly increases the lateral variation in potential energy. Decreasing the spacing between solid atoms makes the potential more nearly constant. As $a_{eff}n_1^{1/2}$ decreases below 0.8, the decrease in corrugation and susceptibility both reduce β leading to a rapid rise in L_s . As $a_{eff}n_1^{1/2}$ increases above 0.8, the increase in corrugation partially offsets the drop in susceptibility and L_s rises

slowly.

Curvature does not affect the spacing along the cylinder axis. This explains why there is almost no change in L_s for axial flow and large changes for radial flow when the nearest-neighbor atoms of a square surface lattice are aligned along the axis. However, when the next-nearest neighbors are along the cylinder axis, L_s changes more for axial flow than radial flow. This change in behavior can be understood by considering how the density modulations produced by the substrate are affected by flow. The largest modulations are at the smallest reciprocal lattice vectors of the substrate \vec{G} . Flow only affects modulations with a component of \vec{G} along the flow velocity \vec{v} . When the nearest-neighbor direction is along the axis there is a reciprocal lattice vector along the axis and another perpendicular. Curvature only affects the perpendicular vector and thus does not affect axial flow. When the next-nearest neighbor direction is along the axis, the reciprocal lattice vectors have both axial and radial components. Curvature rotates the reciprocal lattice vectors towards the axial direction so that axial slip lengths change most (Eq. (24)).

Falk et al. considered axial flow over nanotubes with hexagonal symmetry. In this case the reciprocal lattice vectors are not parallel to the nearest-neighbor spacing. Thus they found large changes for axial flow when the nearest-neighbor direction was along the axis. For this lattice there should be almost no change in axial flow if the nearest-neighbor direction is along the radial direction.

All the observed changes in slip length can be understood in terms of a simple model for friction between the first fluid layer and the substrate [22, 23]. In this model the viscous drag is directly related to $|\hat{G} \cdot \hat{v}|^2$ times the strength of the density modulations produced by the substrate as measured by the in-layer structure factor $S(\vec{G})/N_1$. The changes in structure factor are inverse to the changes in L_s noted above (Fig. 9 and 10(a)). It is largest when $a_{eff}n_1^{1/2}$ is near 0.9 and drops off more rapidly at small a_{eff} because the corrugation becomes weaker as the surface is more closely packed.

The only remaining factor in the theory is the inverse phonon lifetime t_{ph} which describes the rate of energy dissipation out of the density modulations. Numerical data for all surface densities, orientations and interactions collapse onto a universal curve when t_{ph} is plotted against $a_{eff}n_1^{1/2}$ (Fig. 10(b)). The phonon lifetime is largest for $a_{eff}n_1^{1/2} \approx 0.8$ where the fluid can most easily lock into epitaxy with the substrate. When the spacing between fluid atoms is larger or smaller, this locking is difficult and the lifetime decreases. The lifetime is further suppressed by the fact that the density modulations are not uniform across the first layer when spacing between fluid atoms deviates from a_{eff} .

We compared our results to a model proposed by Falk et al. that is also based on the friction between the substrate and first fluid layer [19, 20]. The results are equiv-

alent to the theory of Smith et al.[22, 23] when the potential producing the density modulations is uniform across the two layers (Appendix). This quantitative agreement breaks down for the more realistic potentials used in the main text because the density modulations vary across the first layer. As noted by Falk et al., the exponential decrease in density modulation with height causes quantitative discrepancies between L_s and Eq. (30) by up to an order of magnitude.

Although this study used simple models for both fluid and solid surfaces, the observed trends with curvature should be quite general and the theoretical approach [22, 23] can be extended to more complex cases. Potentially important applications are transport of fluids inside and outside carbon nanotubes [19, 20, 57–61] and other other nanotubes and nanowires. Moreover, many experimental surfaces are rough down to nanometer scales. In this case the effect of topography can not be determined by applying a constant slip length along the surface. There will be intrinsic variations in the local slip boundary condition due to curvature. Including these may explain deviations between past simulations and continuum theories that assume constant L_s [13, 14, 17, 62] and allow construction of a more accurate mesoscopic flow boundary condition.

V. ACKNOWLEDGMENTS

This material is based on work supported by the National Science Foundation under Grants No. DMR-1411144 and DMR-1006805.

VI. APPENDIX

In this appendix we describe simulations that were used to calculate L_s using the models in Refs. [19, 20, 22, 23]. These two dimensional models implicitly assume that the periodic potential from the substrate and the response of the fluid are independent of height within the first layer. In the following we associate the first layer with all atoms in the density peak nearest to the wall. The end of the layer is taken to be the position of the first minimum after the peak in plots like Fig. 3 or 11. All atoms in the first layer feel the same lateral potential from the wall.

The wall-fluid interaction along the z-direction is modeled by a Lennard-Jones 9/3 potential:

$$V(z) = 4\epsilon_{wf} \left[\frac{2}{15} \left(\frac{\sigma}{z} \right)^9 - \left(\frac{\sigma}{z} \right)^3 \right] - V_c, \text{ for } r < r_c, \quad (31)$$

where $\epsilon_{wf} = 0.1\epsilon$ and the potential is zero for $r > r_c$. To model the lateral corrugation of the wall potential, a lateral force was applied only to fluid atoms in the first layer:

$$\vec{F}(x, y) = -\nabla V_1(x, y) \quad , \quad (32)$$

$$V_1(x, y) = 2U_1[\cos(Gx) \sin(\omega t) + \cos(Gy)] \quad , \quad (33)$$

where $G = 2\pi/a$ and the strength of the potential corrugation $U_1 = 0.1\epsilon$. We compare to simulations with flow along the x-direction and the corrugation along this direction varies sinusoidally in time with frequency ω .

The slip length in Eq. (6) is $L_s = \mu/\beta$. To determine β from the theory of Smith et al. we need to calculate the phonon lifetime from Eq. (29). In the limit of small ω , the imaginary part of $\alpha(G, \omega)$ is proportional to ω and the magnitude becomes equal to the real part. In this limit we can use Eq. (25) to write $\omega|\alpha(G, 0)|/\text{Im}[\alpha(G, \omega)] = \omega\text{Re}[n_1(G, \omega)]/\text{Im}[n_1(G, \omega)]$, where $n_1(G, \omega)$ is the areal density modulation in the first layer due to the time dependent corrugation in Eq. 33. We evaluated this ratio for progressively lower frequencies to determine the limiting value for each system. The ratio typically converged for $\omega\tau < 0.001$. Then $|\alpha(G, 0)|$ was determined from the ratio $|n(G, 0)|/U_1$ evaluated in steady state ($\omega = 0$) and t_{ph} was calculated from Eq. (29).

For the ideal wall potential of Eq. (33), we can also quantitatively compare Eq. (28) with the model proposed by Falk et al. [19, 20]. The periodic force in Eq. (30) is $f_1(\vec{G}) = (\vec{G} \cdot \Delta\hat{u})U(\vec{G})$. Thus the only additional quantity to be evaluated is the force decorrelation time

$$t_F = \frac{\int_0^\infty dt \langle F_x(0)F_x(t) \rangle}{\langle F_x(0)F_x(0) \rangle}, \quad (34)$$

where F_x is the total force between the fluid and the substrate along the x-axis. Note that equating the expressions for β from the two theories gives a relation between t_F and t_{ph} :

$$\frac{t_F}{kT} \frac{|\vec{G}|^2 \bar{n}_1^2}{|\alpha(\vec{G}, 0)|^2} S_{1,eq}(\vec{G}) = \frac{1}{t_{ph}(\vec{G}, \vec{G} \cdot \Delta\vec{u})}. \quad (35)$$

Falk et al. note that there is a long tail in the integrand for the force decorrelation time due to hydrodynamic effects. They argue this should not be included in t_F . Following their procedure, we evaluated t_F by taking the plateau value of the integral of Eq. (34). An alternative Green-Kubo relation that avoids long tails has been developed by Huang and Szlufarska [63].

Calculated results for the slip length from both theories are compared to values determined from flow simulations in Fig. 12. All results are equivalent within the statistical errors and show the trends with the ratio of wall atom to fluid atom spacing, $a\bar{n}_1^{1/2}$, that were identified in the main text. The slip length is shortest when the wall spacing and fluid spacing are similar so that the fluid can more readily lock in phase with the substrate. The slip length increases with the mismatch in lengths.

Fig. 12 shows that both two-dimensional theories for L_s are accurate for all wall densities when the physical system is effectively two-dimensional. However, as noted in the main text, atomic surfaces produce a lateral corrugation in potential that can change substantially within

the first layer. The theory of Smith et al. remains quantitatively accurate when the wall and fluid have similar spacings, but predicts too large a phonon lifetime for larger and smaller a . One can view this as a reduction in the lifetime of density modulations that are not coherent across the layer.

We found significant quantitative differences between L_s and the theory of Falk et al. for atomistic surfaces with all spacings. When one evaluates f_1 at the density peak, as they suggest, their model gives values of L_s that are up to an order of magnitude too large. Given the variation in modulation with height one may wonder whether other definitions could improve the quantitative agreement, but we also found a breakdown in the fluctuation-dissipation relation used to derive their expressions. Their starting point is

$$\beta^F = \int_0^\infty dt \langle F_x(0)F_x(t) \rangle / Ak_B T \quad (36)$$

where the left side represents the dissipation, the right side is the fluctuation and the superscript F indicates that this is the prediction of their model. Fig. 13 shows the ratio of β^F to the directly measured value of $\beta = \mu/L_s$. The ratio decreases linearly with a and Eq. (36) is wrong by up to a factor of 2. Of course this does not represent a failure of the fluctuation-dissipation approach, but rather an assumption about how the dissipation is related to flow. Converting β^F to a slip length requires assuming that the first layer is moving coherently and this approximation is invalid because of the rapid change in corrugation potential with height.

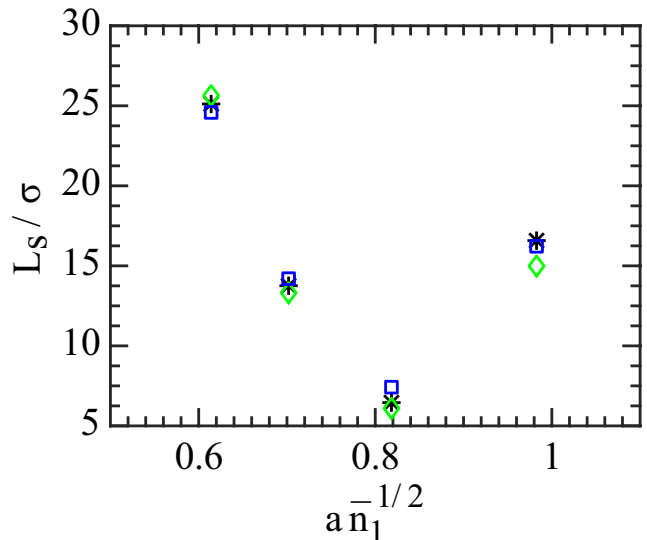


FIG. 12. (Color online) The variation of slip length as a function of the relative wall spacing $a\bar{n}_1^{-1/2}$ for the ideal wall potential of Eq. (32). Asterisks show the slip length determined directly from the Couette profile, diamonds are from the theory of Smith et al. (Eq. (28)), and squares are from the theory of Falk et al. (Eq. (30)). Symbol sizes are comparable to statistical errorbars.

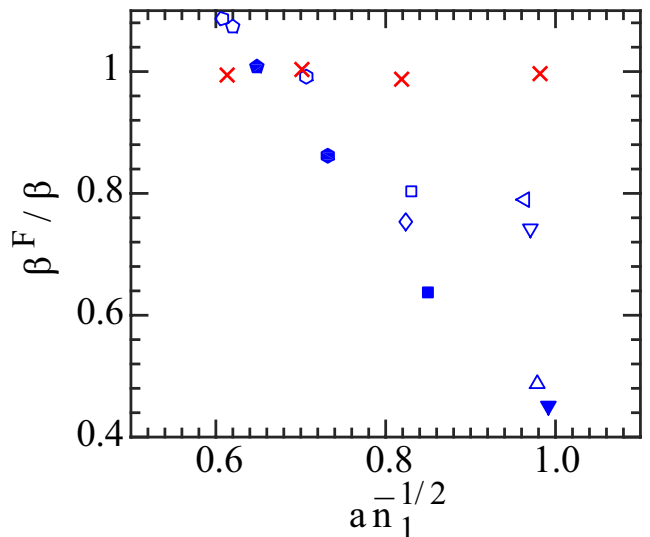


FIG. 13. (Color online) Ratio of the drag predicted by Eq. (36) to the measured drag $\beta = \mu/L_s$ as a function of the relative wall spacing $a\bar{n}_1^{-1/2}$. Red crosses show results for the ideal wall potential of Eq. (32). Blue symbols show results for flow along the (110) direction of flat atomic walls with lattice spacing $a = 1.2\sigma$ (triangles), 1.09σ (circles), 1.00σ (squares), 0.86σ (hexagons) and 0.75σ (pentagons). The symbol type indicates the wall-fluid interaction from Table I: A (open), B (closed), C (right-side left triangle and pentagon) and D (diamond and right-side up triangle).

-
- [1] H. A. Stone, A. D. Stroock, and A. Ajdari, *Annu. Rev. Fluid Mech.* **36**, 381 (2004).
- [2] E. Lauga, M. Brenner, and H. Stone, in *Springer handbook of experimental fluid mechanics* (Springer, 2007) pp. 1219–1240.
- [3] C. Neto, D. R. Evans, E. Bonaccorso, H.-J. Butt, and V. S. Craig, *Reports on Progress in Physics* **68**, 2859 (2005).
- [4] L. Bocquet and J.-L. Barrat, *Soft matter* **3**, 685 (2007).
- [5] C. Denniston and M. O. Robbins, *The Journal of chemical physics* **125**, 214102 (2006).
- [6] C. Navier, *Mémoires de l'Académie Royale des Sciences de l'Institut de France* **6**, 389 (1823).
- [7] P. A. Thompson and M. O. Robbins, *Physical Review A* **41**, 6830 (1990).
- [8] P. A. Thompson and S. M. Troian, *Nature* **389**, 360 (1997).
- [9] M. Cieplak, J. Koplik, and J. R. Banavar, *Physical Review Letters* **86**, 803 (2001).
- [10] T.-M. Galea and P. Attard, *Langmuir* **20**, 3477 (2004).
- [11] N. V. Priezjev, *The Journal of chemical physics* **127**, 144708 (2007).
- [12] N. V. Priezjev, *Physical Review E* **75**, 051605 (2007).
- [13] D. Einzel, P. Panzer, and M. Liu, *Physical review letters* **64**, 2269 (1990).
- [14] P. Panzer, M. Liu, and D. Einzel, *International Journal of Modern Physics B* **6**, 3251 (1992).
- [15] O. I. Vinogradova, *Langmuir* **11**, 2213 (1995).
- [16] E. Bonaccorso, M. Kappl, and H.-J. Butt, *Physical Review Letters* **88**, 076103 (2002).
- [17] N. V. Priezjev and S. M. Troian, *Journal of Fluid Mechanics* **554**, 25 (2006).
- [18] A. Niavarani and N. V. Priezjev, *Physical Review E* **81**, 011606 (2010).
- [19] K. Falk, F. Sedlmeier, L. Joly, R. R. Netz, and L. Bocquet, *Nano letters* **10**, 4067 (2010).
- [20] K. Falk, F. Sedlmeier, L. Joly, R. R. Netz, and L. Bocquet, *Langmuir* **28**, 14261 (2012).
- [21] W. Chen, R. Zhang, and J. Koplik, *Physical Review E* **89**, 023005 (2014).
- [22] M. Cieplak, E. D. Smith, and M. O. Robbins, *Science* **265**, 1209 (1994).
- [23] E. D. Smith, M. O. Robbins, and M. Cieplak, *Physical Review B* **54**, 8252 (1996).
- [24] S. Plimpton, *Journal of computational physics* **117**, 1 (1995).
- [25] G. S. Grest and K. Kremer, *Physical Review A* **33**, 3628 (1986).
- [26] R. Khare, J. J. de Pablo, and A. Yethiraj, *Macromolecules* **29**, 7910 (1996).
- [27] X. Yong and L. T. Zhang, *The Journal of chemical physics* **138**, 084503 (2013).
- [28] N. Tretyakov and M. Müller, *Soft Matter* **9**, 3613 (2013).
- [29] P. Hoogerbrugge and J. Koelman, *EPL (Europhysics Letters)* **19**, 155 (1992).
- [30] P. Espanol and P. Warren, *EPL (Europhysics Letters)* **30**, 191 (1995).
- [31] M. S. Dresselhaus, G. Dresselhaus, and P. C. Eklund, *Science of fullerenes and carbon nanotubes: their properties and applications* (Academic press, 1996).
- [32] T. W. Ebbesen, H. J. Lezec, H. Hiura, J. W. Bennett, H. F. Ghaemi, and T. Thio, *Nature* **382**, 54 (1996).
- [33] R. H. Baughman, A. A. Zakhidov, and W. A. de Heer, *Science* **297**, 787 (2002).
- [34] J. W. Mintmire, B. I. Dunlap, and C. T. White, *Phys. Rev. Lett.* **68**, 631 (1992).
- [35] R. Saito, M. Fujita, G. Dresselhaus, and M. S. Dresselhaus, *Phys. Rev. B* **46**, 1804 (1992).
- [36] R. G. Horn and J. N. Israelachvili, *The Journal of Chemical Physics* **75**, 1400 (1981).
- [37] F. F. Abraham, *The Journal of Chemical Physics* **68**, 3713 (1978).
- [38] S. Toxvaerd, *The Journal of Chemical Physics* **74**, 1998 (1981).
- [39] M. Plischke and D. Henderson, *The Journal of chemical physics* **84**, 2846 (1986).
- [40] I. Bitsanis, S. A. Somers, H. T. Davis, and M. Tirrell, *The Journal of Chemical Physics* **93**, 3427 (1990).
- [41] I. Bitsanis and G. Hadziioannou, *The Journal of chemical physics* **92**, 3827 (1990).
- [42] P. A. Thompson, M. O. Robbins, and G. S. Grest, *Israel Journal of Chemistry* **35**, 93 (1995).
- [43] J.-L. Barrat *et al.*, *Faraday Discuss.* **112**, 119 (1999).
- [44] J. Koplik, J. R. Banavar, and J. F. Willemsen, *Physics of Fluids A: Fluid Dynamics (1989-1993)* **1**, 781 (1989).
- [45] J. Koplik and J. R. Banavar, *Annual Review of Fluid Mechanics* **27**, 257 (1995).
- [46] J. Gao, W. D. Luedtke, and U. Landman, *Physical review letters* **79**, 705 (1997).
- [47] N. V. Priezjev, *Physical Review E* **80**, 031608 (2009).
- [48] N. V. Priezjev, *Physical Review E* **82**, 051603 (2010).
- [49] A. Niavarani and N. V. Priezjev, *Physical Review E* **77**, 041606 (2008).
- [50] L. Bocquet and J.-L. Barrat, *Physical review E* **49**, 3079 (1994).
- [51] N. V. Priezjev and S. M. Troian, *Physical review letters* **92**, 018302 (2004).
- [52] U. Heinbuch and J. Fischer, *Physical Review A* **40**, 1144 (1989).
- [53] See Supplemental Material at [URL will be inserted by publisher] for calculated values of slip length and $\tilde{S}_1(\vec{G})/N_1$ at smallest reciprocal lattice vectors for all the flow geometries and surface properties included in this study.
- [54] M. O. Robbins and M. H. Müser, in *Handbook of Modern Tribology*, edited by B. Bhushan (CRC Press, Boca Raton, 2000 (cond-mat/0001056)) pp. 717–765; M. O. Robbins and M. H. Müser, arXiv preprint cond-mat/0001056 (2000).
- [55] M. O. Robbins and M. H. Müser, in *Modern Tribology Handbook*, edited by B. Bhushan (CRC Press, Boca Raton, FL, 2001) pp. 717–765.
- [56] N. V. Priezjev, *Microfluidics and nanofluidics* **14**, 225 (2013).
- [57] M. Whitby, L. Cagnon, M. Thanou, and N. Quirke, *Nano letters* **8**, 2632 (2008).
- [58] M. Majumder, N. Chopra, R. Andrews, and B. J. Hinds, *Nature* **438**, 44 (2005).
- [59] J. Thomas and A. McGaughy, *Journal of Chemical Physics* **128**, 84715 (2008).
- [60] A. Vanossi, N. Manini, M. Urbakh, S. Zapperi, and E. Tosatti, *Reviews of Modern Physics* **85**, 529 (2013).

- [61] S. K. Kannam, B. D. Todd, J. S. Hansen, and P. J. Davis, *The Journal of chemical physics* **138**, 094701 (2013).
- [62] K. Kamrin, M. Z. Bazant, and H. A. Stone, *J. Fluid Mech* **658**, 409 (2010).
- [63] K. Huang and I. Szlufarska, *Physical Review E* **89**, 032119 (2014).